

Seismic Anisotropy in the upper crust beneath the Sanjiang lateral collision zone in the southeastern margin of the Tibetan Plateau revealed by S wave splitting from a temporary array

Xinyi Li and Yuan Gao*

Key Laboratory of Earthquake Prediction, Institute of Earthquake Forecasting, China Earthquake Administration, Beijing 100036, China

Article history: received June 19, 2022; accepted January 11, 2023

Abstract

The Sanjiang lateral collision zone is a key region to understand the Tibetan Plateau's tectonic structure and the Tethys-Himalayan's tectonic evolution. Complex tectonic structures, intense crustal deformation, frequent seismicity, and abundant metal deposits are all present. With the seismic data recorded by a temporary array (SJ-Array) and permanent stations (Nov. 2018 ~ Dec. 2020), this paper adopts the S wave splitting technique to obtain the essential properties of upper crustal anisotropy. In the interested area, it is shown that the dominant polarization of the fast S wave is NNW, with a mean polarization direction of 167.9° . In addition, the study area can be divided into three subzones from the west to the east: A, B, and C, according to the various mean polarizations varying from NNW, NS to NNE. The mean normalized time delay between the two split S waves is 4.0 ms/km, and the range of time delay is from 2.0 to 6.3 ms/km. The largest time delay is located at the east side of the western boundary of the Sichuan-Yunnan rhombus block. Furthermore, there is a strip area of strong anisotropy stretching along the western segment of the Lijiang-Xiaojinhe fault. These all demonstrate the local tectonic differences and indicate that the crustal structure may be strongly controlled by the fault and block boundary strike.

Keywords: Sanjiang lateral collision zone; Seismic anisotropy in the upper crust; Polarization of fast S wave; Time delay of slow S wave; Deformation

1. Introduction

After four tectonic development stages of evolution of the Proto-, Paleo-, Meso and Neo-Tethys and Indian-Asian plates collision and consequent orogenesis starting in the Cenozoic, in the southeast margin of the Tibetan Plateau developed the Sanjiang lateral collision zone together with the accompanying Sanjiang metallogenic belt [Xu et al., 2012; Pan et al., 2012] (Figure 1). Here Sanjiang in China specially means three rivers (the Nujiang river, the Lancang river and the Jinsha river) run in the narrow zone in this study area. The long evolutionary history resulted

in numerous changes in crustal thickness, and complex deep tectonics in the Sanjiang lateral collision zone, which also makes it an important metallogenic belt in China. This region is an important area to understand the Tibetan Plateau's tectonic growth and the Tethys-Himalayan's tectonic evolution [Tapponnier et al., 1982; Royden et al., 2008; Li et al., 2018].

Seismic anisotropy exists widely in the crust and the upper mantle [Crampin, 1978]. The primary source of anisotropy in the upper crust is the alignment of the stress-induced EDA (Extensive-Dilatancy Anisotropy) micro-cracks [Crampin, 1984; Crampin and Peacock, 2005], in addition to the anisotropy caused by fault and fracture structure and geometry or lithology and anisotropic minerals presence [Müller, 1991; Gao et al., 2011, 2020; Shi et al., 2020; Kaviris et al., 2021]. When the S wave propagates in the anisotropic medium, it splits into two S waves with orthogonal polarizations. These split S waves carry a large amount of information about the properties of the media where waves propagate [Gao et al., 1998; Kaviris et al., 2018]. In the EDA model assumption, the direction of the fast S wave is parallel to that of the vertical EDA cracks, consistent with the direction of maximum principal compressive stress in the region; the time delay of the slow S wave reflects the degree of anisotropy of the seismic wave propagation path [Crampin et al., 1984; Gao et al., 1998]. By analyzing the characteristics of the S wave splitting (SWS), the regional stress field and fault properties can be obtained [Gao et al., 2010, 2014; Kaviris et al., 2017].

In the southeast margin of the Tibetan Plateau, the local anisotropic parameters of the upper crust were obtained through aftershock analysis [Lei et al., 1997; Wu et al., 2004, 2006; Hua et al., 2006]. The regional anisotropic parameters of the upper crust were also obtained in Yunnan or the southeast margin of the Tibetan Plateau using the SWS method of near-field seismic records [Shi et al., 2009; Tai et al., 2015]. Using a temporary linear array in the Sanjiang lateral collision zone, the upper crustal anisotropy characteristics were reported in a small zone across the first-order block boundary (fault zone) using a microseismic identification method, a large amount of effective increased data for SWS was analyzed to obtain the spatial variation characteristics of upper crustal anisotropy, with finer distribution and accuracy [Gao et al., 2019].

This paper focused on the area of the western boundary of the Sichuan-Yunnan rhombus block (SYRB), looking especially at the Lijiang-Heqing wedge (LHW) enclosed by the boundaries of a second-order block (Figure 1). Earthquakes occur frequently in the study area, with the epicenters centered on the boundaries of the blocks. The large deep faults with various orientations meet in the study area. More importantly, the boundaries of first- and second-order blocks cut the study area, dividing it into the Southern Yunnan block (SYB) and Western Yunnan block (WYB) in the west and the SYRB in the east [Zhang et al., 2003]. Clockwise rotation is observed in tectonic stress fields [Sheng et al., 2022] and GNSS data [Jin et al., 2019; Wang and Shen, 2020]. These observations stimulate our interest in the fine anisotropic distributions across the boundary of the first-order block. Anisotropy pattern will help us to better understand the fault properties, the upper crust deformation, and the regional stress field in the study area.

Considering the fact that there are only a few permanent stations in the Sanjiang lateral collision zone and the previous the temporary arrays had short observation periods, the coverage of stations did not meet the needs of crustal anisotropy research at small, local scale. Furthermore, since the SWS data in the upper crust must meet specific criteria, the amount of effective SWS data is often in shortage in areas where the seismic network is not very dense [Liu et al., 2015; Tai et al., 2015]. Thus, to overcome this problem a dense temporary planar array (SJ-Array) was deployed in 2018 to study the structure, crustal deformation, stress distribution, and fault properties in the Sanjiang lateral collision zone, ensuring the data necessary for the study of anisotropy at local scale.

In this study, the near-field seismic waveforms recorded by the SJ-Array (26 stations) and China National Seismic Network (CNSN, 7 stations) from November 2018 to December 2020 were analyzed to extract the SWS parameters and study crustal anisotropy.

2. Tectonic Setting

The central body of the Sanjiang lateral collision zone is located in western Yunnan, China, in the southeast margin of the Tibetan Plateau. The Sanjiang lateral collision zone is an important ore-forming belt in China with a long history of evolution, frequent seismic activity, crustal thickness change, and complex deep tectonics. It is a key region for understanding tectonic development on the Tibet Plateau and tectonic evolution in Tethys-Himalayan system [Tapponnier et al., 1982; Royden et al., 2008; Li et al., 2018].

The continental collision between Eurasian and Indian plates and the large-scale slide have resulted in this region in a clockwise rotation and in the formation of the strike-slip shear zones of the Sanjiang, as well as the red

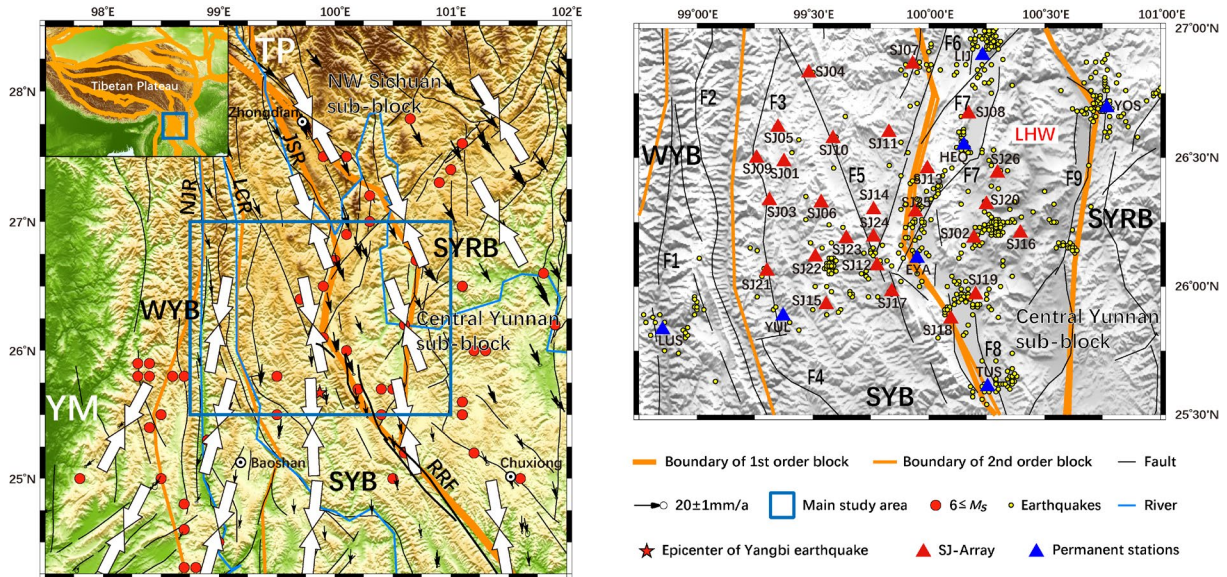


Figure 1. Tectonic background, seismic stations, and historical earthquakes. Map on the left – The red dots represent the epicenters of historical earthquakes of $M_S \geq 6.0$ (before January 15, 2022). The star represents the Yangbi $M_S 6.4$ earthquake on May 21, 2021. Block boundaries are represented by the orange lines [from Zhang et al., 2003]. The blue lines represent the Nujiang river (NJR), the Lancang river (LCR) and the Jinsha river (JSR). Jin et al. [2019] provides the GPS velocity field data relative to the Eurasian plate (small black arrows). The white arrows in pairs represent the stress field direction [from Sheng et al., 2022]. TP (Tibetan Plateau) and YM (Yunnan-Myanmar block), white labels, represent the first-order blocks. SYRB (Sichuan-Yunnan rhombus block), SYB (Southern Yunnan block), and WYB (Western Yunnan block), black labels, represent the second-order blocks. RRF represents the red river fault. The blue frame in the left diagram shows the area of the map in the right diagram. The inset in the upper left corner show the position of the studied area relatively to the Tibetan Plateau. Map on the right- The second order block labels are shown. LHW represents the Lijiang-Heqing wedge. Faults are represented by the dark lines: from west to east. F1, Nujiang fault; F2, Lancang river fault; F3, Lanping-Yunlong fault; F4, Yongping fault; F5, Weixi-Qiaohou-Weishan fault; F6, Longpan-Qiaohou fault; F7, Lijiang-Xiaojinhe fault; F8, Eryuan-Midu fault; F9, Chenghai fault [from Xu et al., 2016]. The red and blue triangles, respectively, show the temporary and permanent stations. The yellow dots represent the epicenters of earthquakes with records in the S wave window analyzed in this study.

river strike-slip fault zone and the Lancang river strike-slip fault zone [Yin et al., 2021]. The upper crust deformation features in these zones are dominated by the lateral slip, while on the Tibetan Plateau forward collision is the dominant mode of deformation [Li et al., 2018]. GPS observations [Jin et al., 2019] indicated the changing pattern of the surface movement in an overall clockwise rotation around the East Himalayan tectonic knot: in the study area (Figure 1, black small arrows) the surface movements point SE in the northern region, while to pointing to S in the central region, to pointing to SSW in the southern area. The focal mechanisms of earthquakes in the region [Wu et al., 2004; Qian et al., 2011; Sun et al., 2017; Tian et al., 2019] show complexity: mainly compression mechanisms but also a large number of strike-slip earthquakes, accompanied by normal types. The stress field derived from the focal mechanisms of small and medium-sized earthquakes (magnitude 1.0 to 5.0) [Xu et al., 1987; Wu et al., 2004], as well as some strong earthquakes [Kan et al., 1977; Qian et al., 2011; Sheng et al., 2022] is shown by white arrows in Figure 1. In the region where the seismic stations were deployed (Figure 1 map on the right) in the northern region there is a NNW principal compressive stress direction, while the compressional axis rotate to nearly NS in the southern part of the studied region. The crustal thickness changes considerably in this small area, ranging from 40 to 62 km. According to the inversion results of the teleseismic receiver functions, it gradually thinned from about 60 km in Zhongdian to 40 km in Baoshan, Chuxiong, and other southern regions [Wu et al., 2001; Hu et al., 2003; He et al., 2004; Zhang and Gao, 2019]. Lithospheric anisotropy in the study area is characterized by lateral zoning and vertical stratification. The dominant polarization of fast S waves in the upper crust is in a nearly NS direction, but laterally it is zoned in the smaller local area, which is in good agreement with the surface deformation

and principal compressive stress direction. In the middle and lower crust, the fast S waves have approximately the same orientation as in the upper crust, which is a nearly NS or NNW direction. The anisotropy of the lithosphere is characterized by north-south zoning, and $26^{\circ}20'N$ is an essential dividing line [Gao et al., 2020]. On the north side, the fast S wave polarizations in the upper crust and in the lithosphere are both in NS. On the south side, however, the fast S wave polarizations of the lithosphere change directions into the EW.

Large-scale strike-slip faults are not only crucial in the creation of the Sanjiang lateral collision zone, but they also serve as sources of earthquakes and a conduit for ore-forming fluid [Xu et al., 2012]. More than 200 earthquakes of $M \geq 5.0$ were recorded in western Yunnan during the twentieth century, far more than in other zones of China [Huangfu et al., 2000]. Historically, six large earthquakes of $M \geq 7.0$ occurred within the Sanjiang lateral collision zone, including the Yongsheng M 7.8 earthquake in 1515, the Midu M 7.0 earthquake in 1652, the Dali M 7.0 earthquake in 1925, the Longling M_S 7.3 and M_S 7.4 earthquakes in 1976, and the Lijiang M_S 7.0 earthquake in 1996. On May 21, 2021, an M_S 6.4 earthquake struck Yangbi County, Dali, Yunnan Province, which caused casualties. In addition, the Sanjiang lateral collision zone is a vital mineralization zone in China, as it is where the significant copper ore and other rich metal ores are currently distributed [Deng et al., 2010; Li et al., 2018].

3. Data and method

3.1 Data

This study uses the seismic records from the SJ-Array (i.e., temporary Sanjiang planar seismic Array) and CNSN stations (Figure 1). The SJ-Array was a temporary planar array set up by the Institute of Earthquake Forecasting, China Earthquake Administration, in November 2018 in the Sanjiang area. It consists of 26 stations equipped with Nanometrics instruments (Trillium-120 seismometer and Taurus data acquisition). Operating for 2 years, through 2020 in the region of the western boundary of the SYRB, the stations were spaced less than 20 km apart, forming a “planar” array (SJ01-SJ26), different from the earlier “linear” seismic array: the SL-Array [Gao et al., 2019]. Within the study area, there are four permanent stations (YUL, EYA, HEQ, and LIJ). Another three permanent stations (LUS, YOS, and TUS) are near the SJ-Array.

This paper uses the near-field seismic waveform data recorded by the SJ-Array and CNSN stations between November 2018 and December 2020. A total of 2284 seismic events below M_L 4.0 were obtained in the study area during the observation period, according to the earthquake catalog provided by the China Earthquake Networks Center (CENC). This study adopts the S wave window of 45° incidence [Booth and Crampin, 1985; Gao et al., 2019], and 856 earthquake waveform records were finally obtained within the S wave window.

3.2 Method

The systematic analysis method (SAM) is an SWS technique based on the correlation function that combines correlation function calculation, time delay correction, and polarization analysis experiments [Gao and Zheng, 1995; Gao et al., 1998]. Objectivity and accuracy are strong, as is self-measurement [Shi et al., 2009]. Practical examples of data processing are shown in Figure 2 and Figure 3.

Figure 2 shows the three-component seismic waveforms recorded at station SJ19 after processing with a four-order Butterworth bandpass filter with cutoff frequencies of 1-10 Hz. This seismic event ($M_L = 0.3$) occurred on Feb. 1, 2019, with a focal depth of 12 km and an epicentral distance of 10.9 km.

The polarization analysis diagram of the S wave horizontal components and the polarization analysis check diagram are shown in Figure 3, respectively. The particle movement trajectory of the S wave, i.e., the polarization diagram, is generally linear in the period between the arrival of the fast and slow S wave (see line S_1S_2 in Figure 3(a)). The direction of this linear trajectory is at an angle θ with the due north, which is the polarization direction of the fast S wave. The slow S wave then arrives and superimposes itself on the fast S wave, altering the particle movement's trajectory.

The SAM method can separate fast and slow S waves by rotating the NS and EW components simultaneously at an angle θ . After rotation, the slow S wave is set at an earlier time Δt to eliminate the effect of time delay. The Δt is the time difference between the fast and slow S wave, i.e., the time delay. At this point, the initial time of the slow

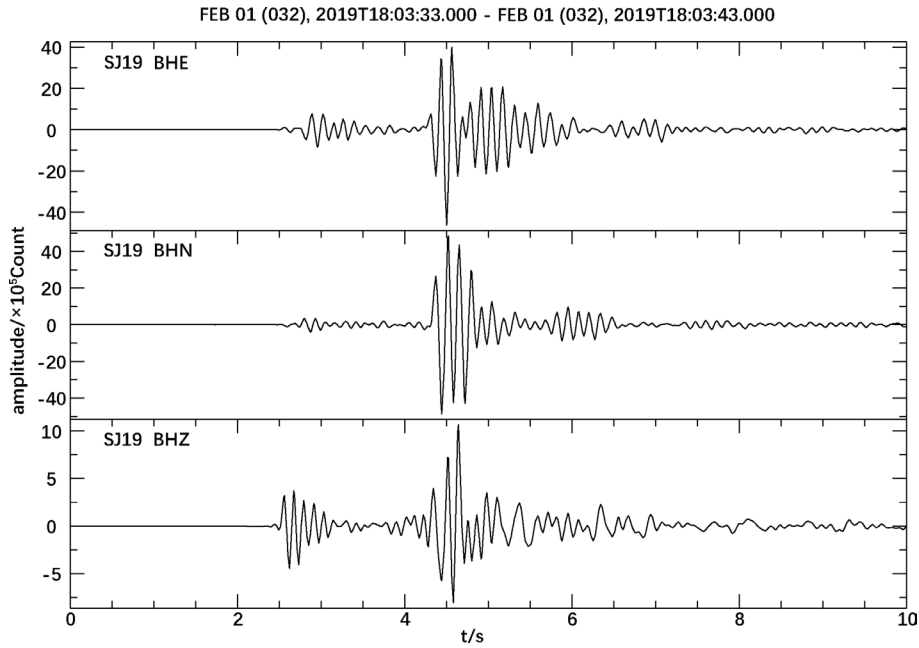


Figure 2. Seismic waveforms at station SJ19. The three-component waveforms of a small earthquake ($M_L = 0.3$) were recorded at station SJ19 on Feb. 1, 2019, with a focal depth of 12 km, and an epicentral distance of 10.9 km. The waveforms from the top to the bottom in the figure are the EW, NS, and vertical components, respectively. The horizontal coordinate (X-axis) indicates the time in seconds, and the vertical coordinate (Y-axis) indicates the amplitude in counts.

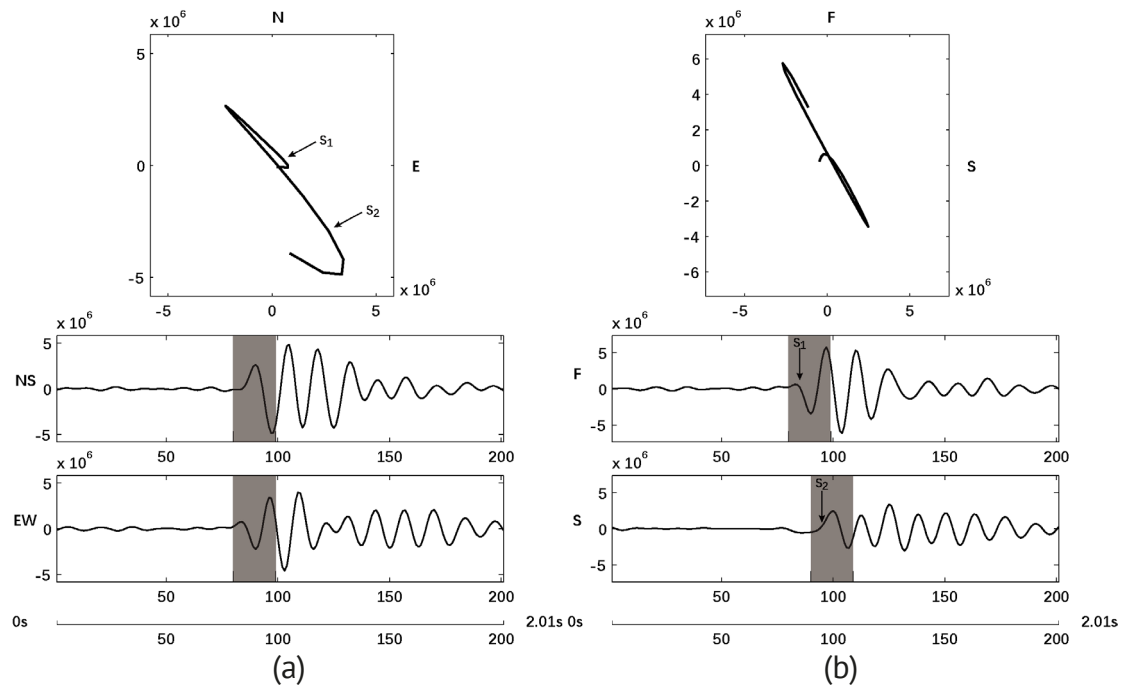


Figure 3. Polarization analysis of SWS. (a) Analytical diagram of the horizontal component polarization of S waves. The upper panel shows the trajectory of the S wave particles, and the plotted data corresponds to the shaded area in the lower panel; S_1 and S_2 are the initial arrival points of fast and slow S waves, respectively; the lower panel shows the S waves of NS and EW components, respectively; the horizontal coordinate (X-axis) indicates the number of sampling points, and the vertical coordinate (Y-axis) indicates the amplitude count value. (b) Polarization analysis test diagram after time delay correction. After eliminating the time delay, good linearity of the S wave particle trajectory is shown in the upper panel. The lower panel shows the fast (F) and slow (S) S waves, the rest are consistent with (a). The polarization direction is 132° , and the time delay is 0.1 s.

S wave is the same as that of the fast S wave, and the polarization diagram should return to linearity. Figure 3(b) displays the polarization analysis result after subtracting the time delay. The polarization diagram becomes linear after setting the slow S wave ahead of time by Δt , demonstrating the accuracy of the measured results.

4. SWS parameters and spatial variations

The SWS parameters in the study area were first estimated by the temporary planar SJ-Array and permanent stations, based on the earthquake catalog from the CENC, using near-field seismic waveform data. After calculating and analyzing 856 seismic waveforms recorded within the S wave window of incident angle 45° , we obtain the fast S wave polarization directions and the time delays at 23 stations (Table 1 and Table 2).

Station codes	No. of events	Mean fast polarizations \pm errors/ $^\circ$	Mean normalized time delays \pm errors/(ms·km $^{-1}$)
SJ12	5	158 \pm 8.6	2.8 \pm 1.1
SJ15	5	170.2 \pm 17.3	3.4 \pm 3.4
SJ16	13	10.8 \pm 29.8	2.0 \pm 1.2
SJ17	3	179.3 \pm 25	4.4 \pm 2.4
SJ18	14	11.6 \pm 21.3	2.7 \pm 1.6
SJ19	3	178 \pm 45.5	4.7 \pm 1
SJ20	3	50.7 \pm 25.4	2.6 \pm 0.4
SJ22	75	153.7 \pm 21.4	4.2 \pm 1.7
SJ23	6	145.8 \pm 10.5	2.4 \pm 1
EYA	17	0.6 \pm 35.2	5 \pm 3.4
HEQ	11	13.5 \pm 14.1	6.3 \pm 3.3
YOS	9	10.4 \pm 26.4	3.7 \pm 1.7

Table 1. SWS parameters at stations with 3 or more measurements

Station codes	No. of events	Mean fast polarizations \pm errors/ $^\circ$	Mean normalized time delays \pm errors/(ms·km $^{-1}$)
SJ02	1	20	0.7
SJ04	1	136	5.7
SJ07	1	133	1.6
SJ08	1	22	-
SJ11	2	170.5 \pm 13.4	2 \pm 0.7
SJ21	2	36.5 \pm 43.1	4.7 \pm 0.6
SJ25	1	128	2
LIJ	1	15	7.1
LUS	1	161	3.2
TUS	1	84	0
YUL	2	130.5 \pm 7.8	2.7 \pm 0.1

Table 2. SWS parameters at stations with only 1 or 2 measurements.

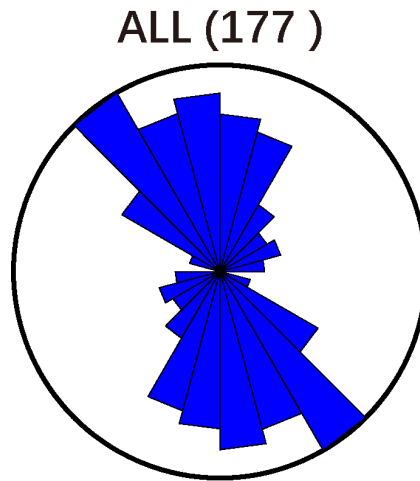


Figure 4. Equal-area projection rose diagram of the fast S wave polarizations in the study area.

Twelve of these stations have effective records (defined as available to SWS parameters within the S wave window, with clear waveforms) larger than or equal to three (Table 1). The results of other stations with fewer than three effective records are shown in Table 2 and Figure 5(a). The equal-area projection rose diagram of the fast S wave polarization of all effective SWS parameters in the study area is shown in Figure 4. The mean fast S wave polarization direction is 167.9° in the whole study area, which agrees well with the pattern of the GPS horizontal

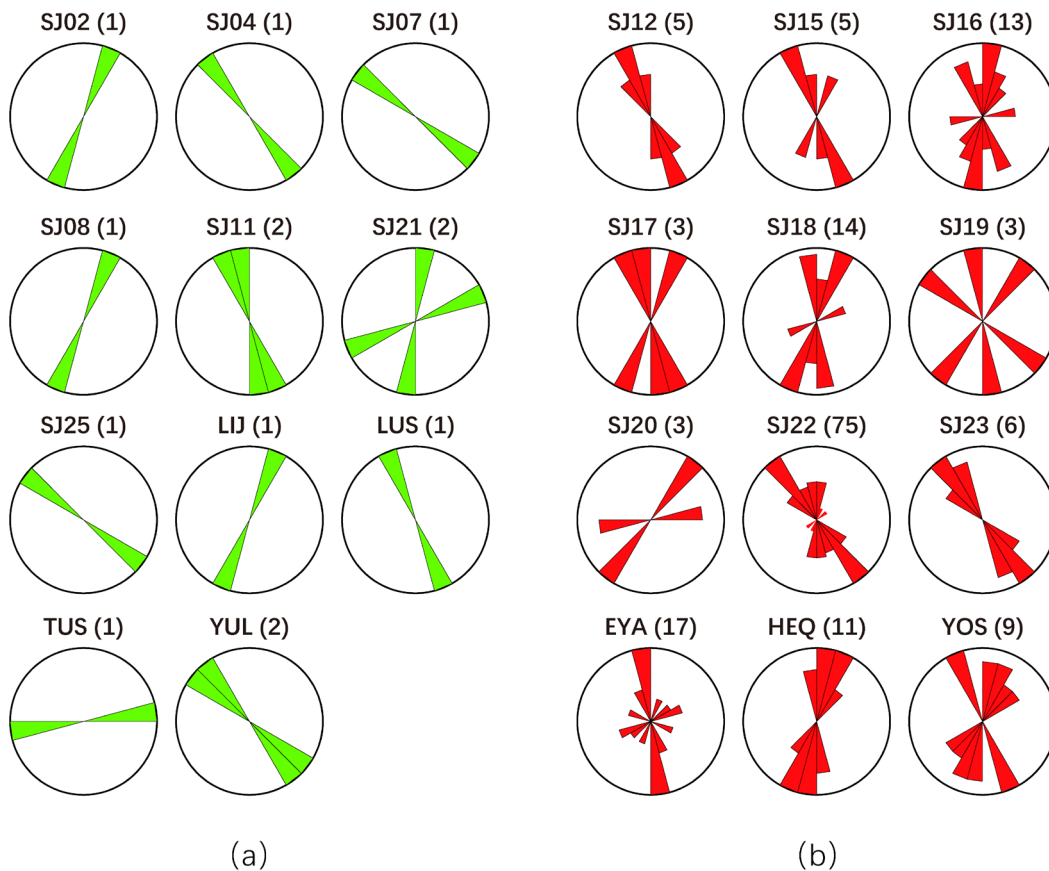


Figure 5. Rose frequency diagrams of fast S wave polarizations at each station. The equal-area projection rose diagrams of fast S wave polarizations at each station are represented by the circle plot. Each rose diagram is labeled with the station code and the number of effective records in parentheses. (a) Stations with only 1 or 2 effective records. (b) Stations with 3 or more effective records.

velocity field [Jin et al., 2019]. The stress data [Kan et al., 1977; Sheng et al., 2022; Tian et al., 2019] also indicated that the regional principal compressive stress is in an NNW direction in the study area.

When the equal-area projection rose for each station is plotted, it is clear that most of the stations, such as SJ12, SJ22, SJ23, HEQ, etc., have good consistency in the dominant S wave polarization (Figure 5(b)). However, some of the stations, such as SJ19 and SJ20, have only three effective records and are relatively scattered. Only a small number of earthquakes occurred in the northwestern region of the study area (see Figure 1 map on the right), this may explain the lack of effective records at stations SJ01, SJ03, SJ05, SJ06, SJ09, and SJ10.

4.1 Polarizations of fast S waves

The spatial distribution of the fast S wave polarizations in the Sanjiang lateral collision zone presents obvious zoning features. From the west to the east, the study area can be divided into three subzones, i.e. A, B, and C (Figure 6). Table 3 presents the SWS results for three subzones.

In subzone A, the NNW-oriented Nujiang fault (F1), Caojian fault, Lancang river fault (F2), Lanping-Yunlong fault (F3), Yongping fault, and Weixi-Qiaohou-Weishan fault (F5) are scattered from the left to the right, roughly in the west side of the Weixi-Qiaohou-Weishan fault (Figure 7). The Nujiang fault, Lancang river fault, and Weixi-Qiaohou-Weishan fault are all dominated by strike-slip [Li et al., 2021; Wang et al., 2022], and the results of the focal mechanism also indicate that the region is dominated by strike-slip earthquakes [Li and Gao, 2022]. In this part of

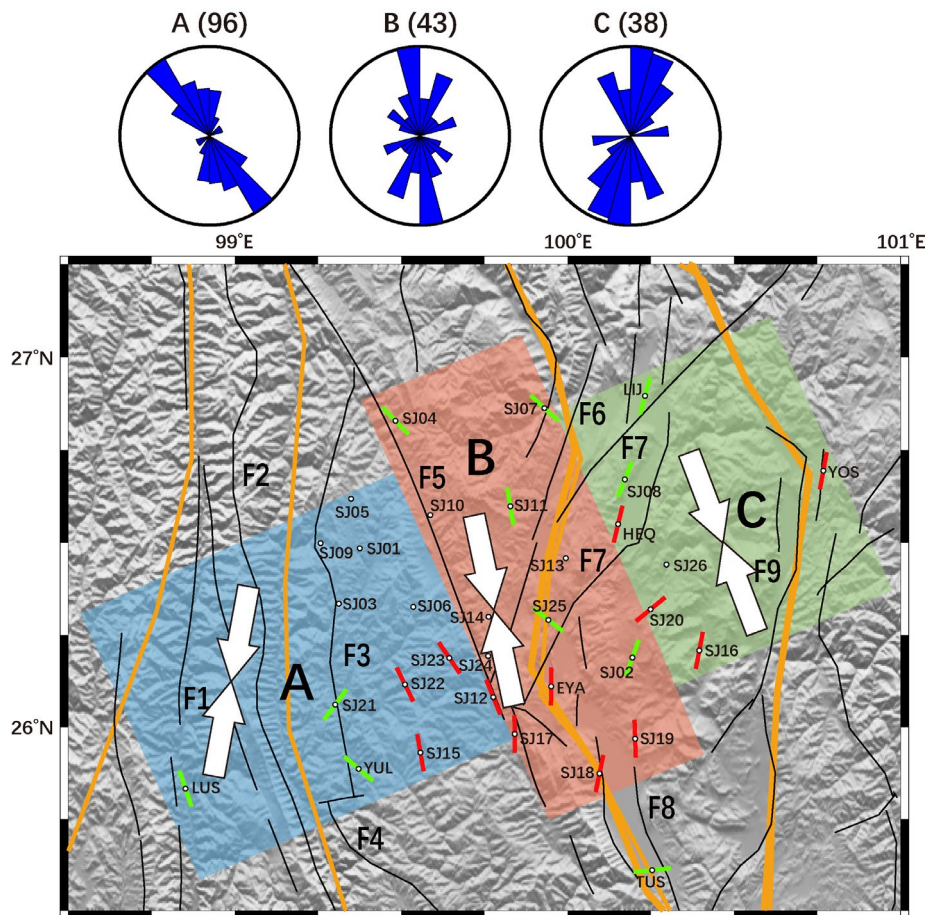


Figure 6. Mean fast S wave polarizations at stations and rose diagrams in the subzones. The directions of the straight lines in this figure are the mean fast S wave polarizations at stations. The red lines indicate the results at stations with 3 or more effective records, and the green lines indicate the results with only 1 or 2 effective records. The three blue equal-area projection rose diagrams on the top of this figure show the dominant fast S wave polarizations in the three subzones. Others are the same as in Figure 1.

Subzone	No. of effective records	Mean fast polarizations \pm errors/($^{\circ}$)	Mean normalized time delays \pm errors/(ms \cdot km $^{-1}$)
A	96	151.4 \pm 22.7	4 \pm 1.8
B	43	0.6 \pm 31.1	3.8 \pm 2.7
C	38	15.1 \pm 25.4	4.1 \pm 3

Table 3. The SWS parameters in three subzones.

the study area, there are ten temporary and two permanent stations. The dominant polarization of this area is an NNW direction (Figure 6), with a mean fast S wave polarization of 151.4 $^{\circ}$ (Table 3), which is compatible with the regional surface motion direction [Jin et al., 2019] and the principal compressive stress direction [Kan et al., 1977; Sheng et al., 2022; Tian et al., 2019].

Stations between faults F3 and F5, stations SJ15, SJ22, and SJ23, are far away from the faults, so the polarizations of these stations represent the direction of local principal compressive stress. Stations SJ22 and SJ23 are equally polarized at about 150 $^{\circ}$. The dominant polarization of station SJ15 shows an NNW direction parallel to the regional maximum principal compressive stress direction, but the NNE direction is also recorded. The mean polarization at station SJ12 is 158 $^{\circ}$, parallel to fault F5, which is almost beneath the station. Station SJ12 owns 5 effective records with conspicuous consistency. It suggests strong impacts by the large deep fault.

Subzone B is a strip area east of the Weixi-Qiaohou-Weishan fault (F5), around the western boundary of the SYRB (Figure 8). There are several large deep faults intersecting in this area, including the NNW-oriented Weixi-Qiaohou-Weishan fault (F5) and the Eryuan-Midu fault (F9), the NNE-oriented Longpan-Qiaohou fault (F6)

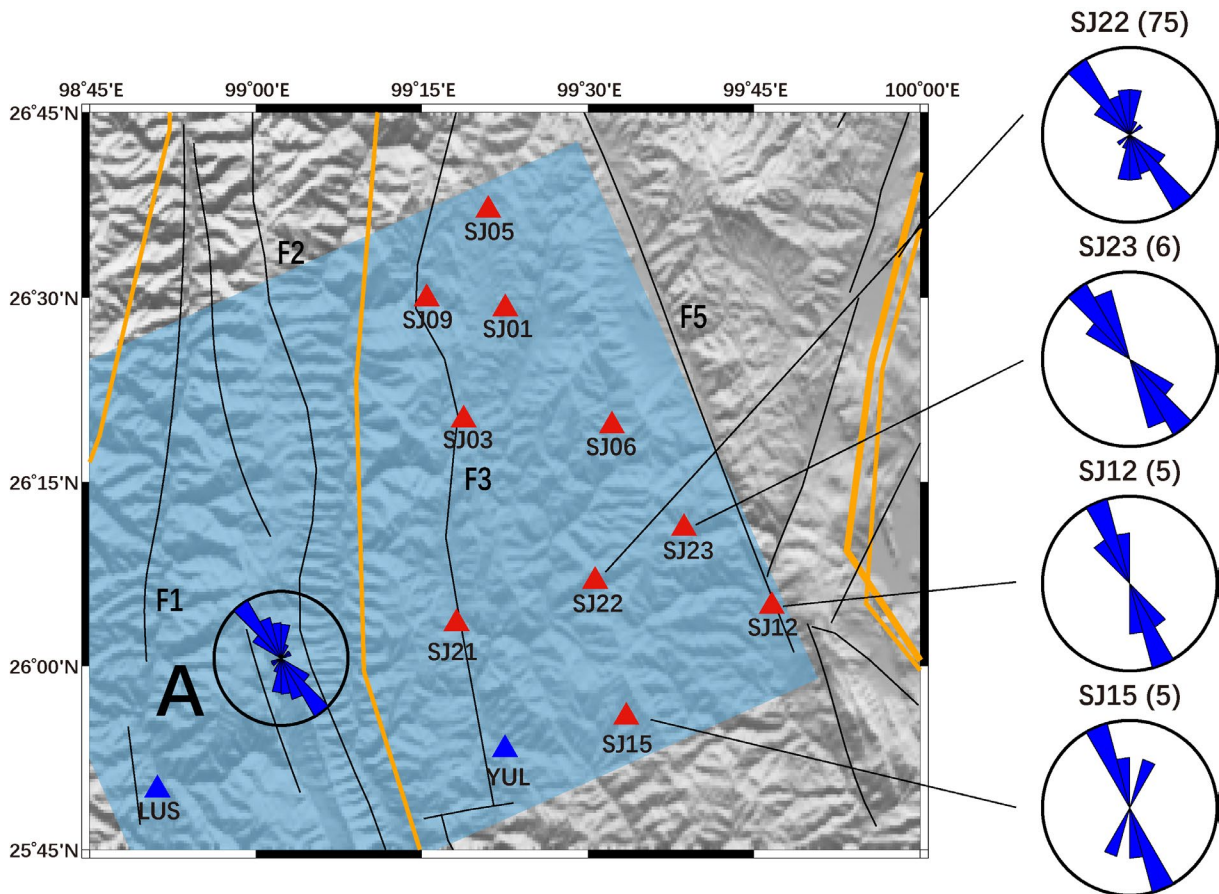


Figure 7. Equal-area projection rose diagrams of fast S wave polarizations at each station in subzone A. The inset A is the equal-area projection rose diagram of fast S wave polarizations in subzone A. Others are the same as in Figure 1.

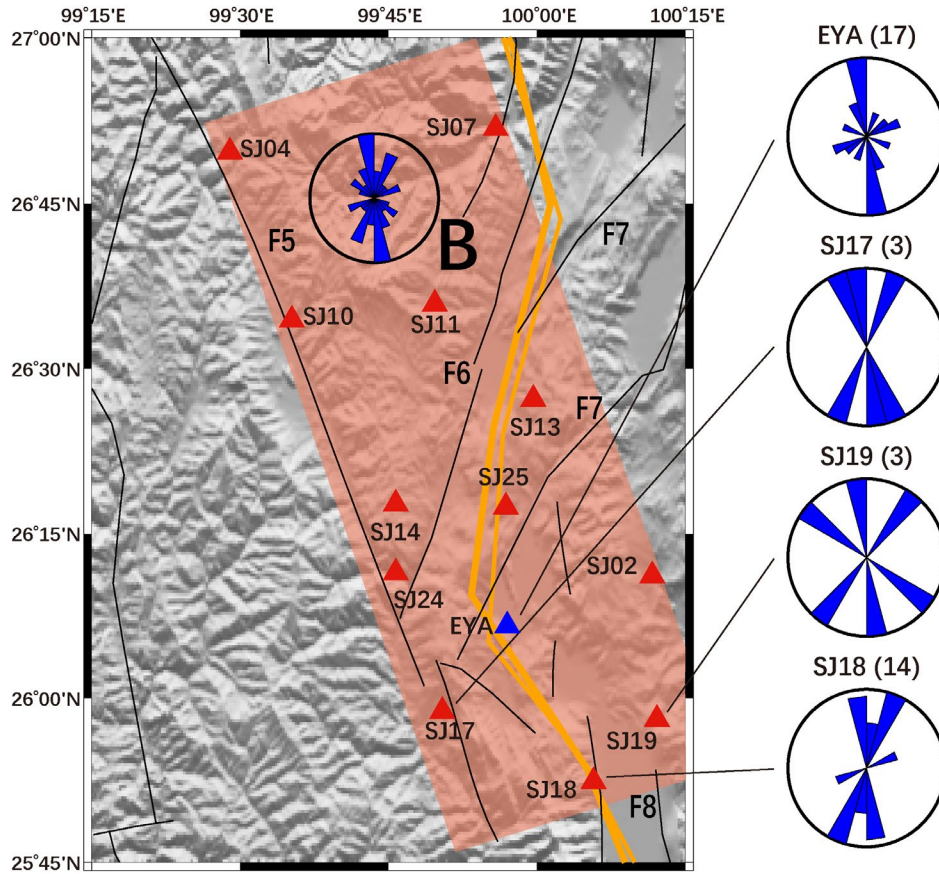


Figure 8. Equal-area projection rose diagrams of fast S wave polarizations at each station in subzone B. The inset B is the equal-area projection rose diagram of fast S wave polarizations in subzone B. Others are the same as in Figure 1.

and the Lijiang-Xiaojinhe fault (F7) [Xu et al., 2016]. In subzone B, there are twelve temporary stations and one permanent station. The dominant polarization is nearly in NS (Figure 6), and the mean fast S wave polarization is at 0.6° (Table 3), similar to that of Gao et al. [2019].

Station SJ17 near fault F5 contains only three effective records with a nearly NS mean polarization direction but relatively scattered. Station SJ18 is close to the nearly NS-oriented faults, with a mean polarization direction of 11.6° . Station EYA is located near the boundary of the block, not far from the fault, with a distinct dominant polarization direction near NS and a second direction near NE (Figure 8). The dominant polarization direction of station EYA is parallel to the western boundary of the SYRB to its left, and the second direction is the same as the fault F7 strike. The mean polarization direction of the Station SJ19 is 178° , parallel to the regional principal compressive stress direction, but only three effective records are available and scattered.

Subzone C is located in the eastern part of the study area, i.e., the LHW, as a part of the SYRB. The nearly NE-oriented Lijiang-Xiaojinhe fault (F7) and the NNE-oriented Chenghai fault (F9) cut this area. The dominant polarization of the fast S waves is at an NNE direction (Figure 6), and the mean fast S wave polarization is 15.1° (Table 3).

The mean polarization direction of both stations SJ16 and HEQ is all in NNE, which is conspicuously influenced by the adjacent large deep fault F7. Station YOS is close to fault F9. The mean polarization direction is parallel to the fault. Nevertheless, because of the adjacent fault and block boundary, YOS also shows an NNW polarization direction.

4.2 Time delays of slow S waves

The time delay between the two split shear waves represents the degree of anisotropy in the seismic wave propagation path [Crampin et al., 1984; Gao et al., 1998]. The mean normalized time delays (time delay per ray path length) were between 2.0 and 6.3 ms/km (Figure 10, Table 1) and 4.0 ms/km for the entire study area. The mean

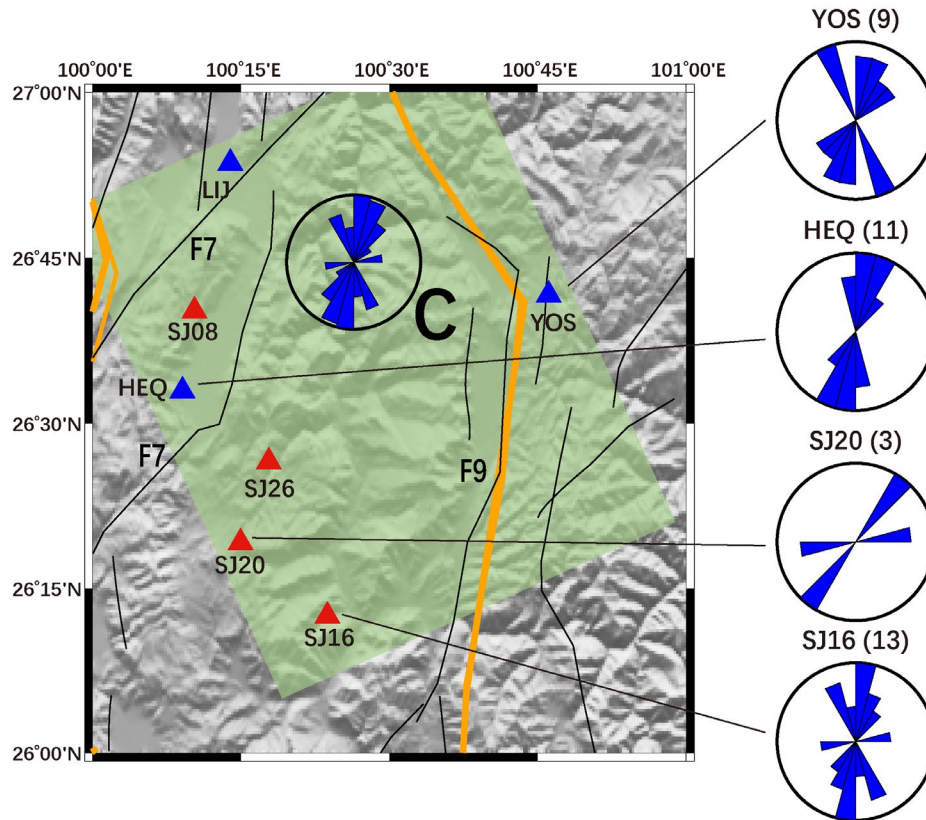


Figure 9. Equal-area projection rose diagrams of fast S wave polarizations at each station in subzone C. The inset C is the equal-area projection rose diagram of fast S wave polarizations in subzones C. Others are the same as in Figure 1.

normalized time delay in the three subzones is close to each other (Table 3). The largest time delay is in subzone C, followed by the time delay in subzone A. The lowest time delay is in subzone B.

The spatial smoothness of the time delays at the station (i.e., meshing data using adjustable tension continuous curvature splines) reveals a clearer spatial distribution of time delays, indicating strong or weak anisotropy in the upper crust of the study area (Figure 11). It shows the spatial distribution of strong anisotropy within the Sanjiang lateral collision zone, i.e., the strong deformation area in the upper crust (the area I and II in Figure 11).

Area I is the intersection of significant faults, such as F5, F6, and F7 (Figure 11). More importantly, the first-order block boundary cuts the area I. It suggests considerable crustal deformation due to the stress effect. Area II is cross the Lijiang-Xiaojinhe fault (Figure 11), with a marked thinning of the crustal thickness from north to south [Wu et al., 2001; Hu et al., 2003; He et al., 2004; Zhang and Gao, 2019]. The tectonic geomorphic study shows that the tectonically active area in the Central Yunnan sub-block (Figure 1) is concentrated in the area near the Lijiang-Xiaojinhe fault and the red river fault [Wang et al., 2021]. The results show that seismic activity, stress concentration, and strong crustal deformation are strong at the junction of the Lijiang-Xiaojinhe fault and the west boundary of the SYRB.

In addition, this study reveals an interesting phenomenon (Figure 11): these stations of large time delays seem to form a strong deformation belt. This uncovers the strong influence of the Lijiang-Xiaojinhe fault.

5. Conclusions

In this study, the near-field seismic waveform data recorded by the SJ-Array (26 stations) and the CNSN permanent stations (7 stations) from November 2018 to December 2020, were used to initially determine the SWS parameters in the study area using the SAM technique [Gao and Zheng, 1995].

Twenty-three stations provided 177 effective SWS parameters, including the fast S wave polarization directions and the time delays. The dominant polarization of the Sanjiang lateral collision zone is in an NNW direction, and

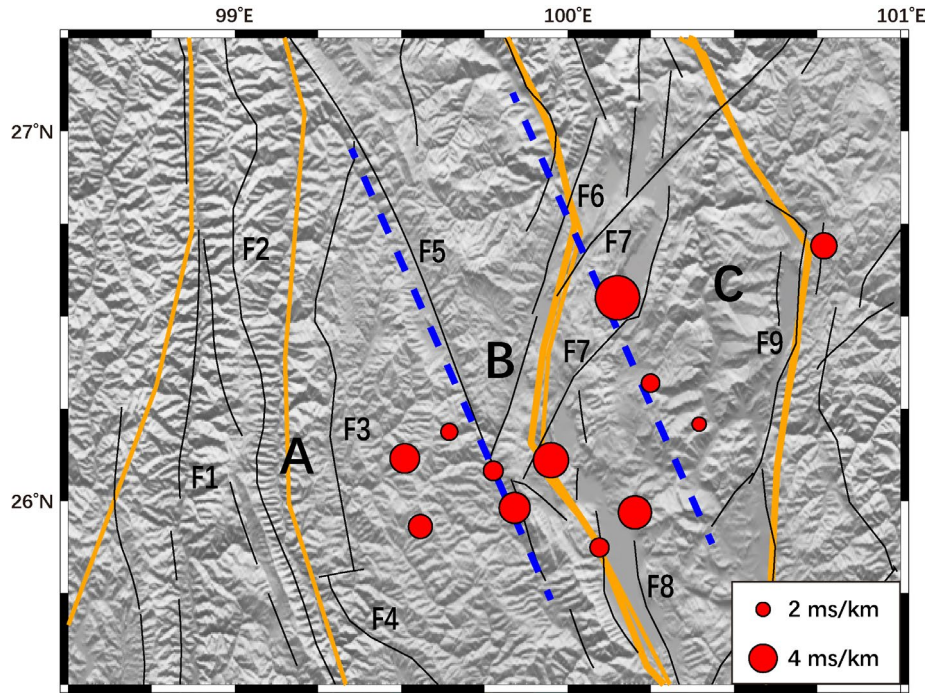


Figure 10. Mean time delays at stations. The red solid circles represent the mean time delays of stations with three or more effective records. The radius of the circles is proportional to the value of the time delays. Others are the same as in Figure 1.

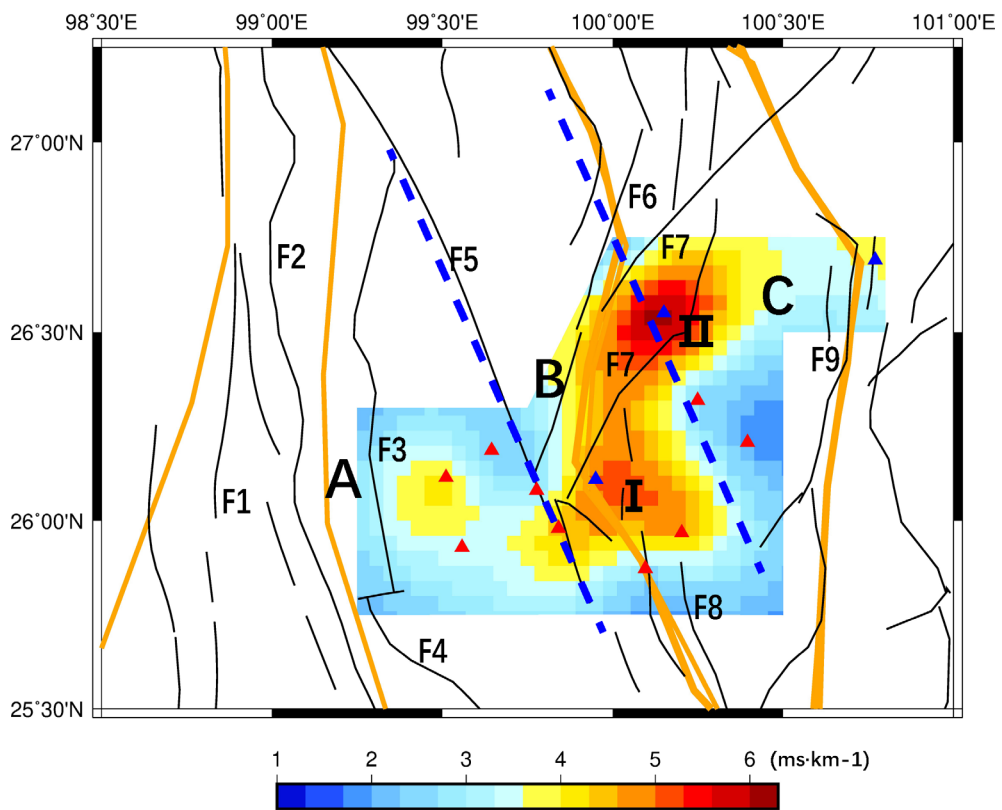


Figure 11. Spatial distribution of time delays in the Sanjiang lateral collision zone.

the mean polarization is about 167.9° , which is in good agreement with the surface motion direction determined by the GPS horizontal velocity field [Jin et al., 2019], as well as the fast S wave direction [Gao et al., 2019] and the compressive axes of the stress field determined by inversion of the focal mechanisms [Kan et al., 1977; Sheng et al., 2022; Tian et al., 2019].

Furthermore, this study obtained a fine anisotropic distribution across the boundary of the first-order block. We divided the study area into three major subzones A, B, and C, from west to east, with the fast S wave polarization direction varying gradually from NNW to NS to NNE, clockwise. In subzone A, the dominant polarization is in an NNW direction, and the mean fast S wave polarization is 151.4° , which is compatible with the regional surface motion and principal compressive stress direction. The fault and the block boundary distinctively affect the fast S wave polarization in subzone B. The overall dominant polarization is around NS. The Lijiang-Xiaojinhe fault controls the fast S wave polarization direction in subzone C. Different from the direction of the regional stress field, the dominant polarization direction of fast S waves in subzone C is in NNE direction, and the mean polarization is 15.1° . The mean normalized time delay in the study area is 4.0 ms/km, ranging from 2.0 to 6.3 ms/km. The time delay in subzone C is the largest, followed by subzone A, and the lowest in subzone B. Furthermore, there is a strip area of strong anisotropy, seemingly stretching along the western segment of the Lijiang-Xiaojinhe fault, ceasing around the western boundary of the SYRB. These all demonstrate the local tectonic differences and indicate that the crustal structure may be strongly controlled by the fault and block boundary strike.

Due to the very stringent data criteria, the amount of effective data accessible for SWS is quite limited so the effective records are low. For SWS, microseismic data can provide more analyzable events. The results of the SWS demonstrate that the waveforms of microseismic events are of excellent quality, and the results are pretty reliable [Gao et al. 2019]. The dominant fast S wave polarization direction determined by microseismic data is extremely compatible with the results determined by seismic data from the public earthquake catalog [Gao et al. 2019]. To achieve more precise anisotropy results in the small-scale area, it is important to enhance the amount of effective data via microseismic identification in the local tectonic regions such as the Sanjiang lateral collision zone.

Acknowledgments. This study is supported by the National Natural Science Foundation of China (Project 41730212) and the Special Fund of Key Laboratory of Earthquake Prediction, CEA (Project 2021IEF0103). We sincerely appreciate the editors and the two reviewers for their thoughtful comments and suggestions, which helped us to improve this manuscript greatly. The earthquake catalog was from the China Earthquake Networks Center. The figures were drawn using GMT.

References

- Booth, D. C. and S. Crampin (1985). Shear-wave polarizations on a curved wavefront at an isotropic free surface, *Geophys. J. Int.*, 83, 1, 31-45, doi: 10.1111/j.1365-246X.1985.tb05154.x.
- Crampin, S. (1978). Seismic-wave propagation through a cracked solid: Polarization as a possible dilatancy diagnostic, *Geophys. J. Int.*, 53, 3, 467-496, doi: 10.1111/j.1365-246X.1978.tb03754.x.
- Crampin, S. (1984). Effective anisotropic elastic constants for wave propagation through cracked solids, *Geophys. J. Int.*, 76, 1, 135-145, doi: 10.1111/j.1365-246X.1984.tb05029.x.
- Crampin, S. and S. Peacock (2005). A review of shear-wave splitting in the compliant crack-critical anisotropic Earth, *Wave Motion*, 41, 1, 59-77, doi: 10.1016/j.wavemoti.2004.05.006.
- Crampin, S., E. M. Chesnokov and R. G. Hipkin (1984). Seismic anisotropy-the state of the Art: II, *Geophys. J. Int.*, 76, 1, 1-16, doi: 10.1111/j.1365-246X.1984.tb05017.x.
- Deng, J., Z. Hou, X. Mo, L. Yang, Q. Wang and C. Wang (2010). Superimposed orogenesis and metallogenesis in Sanjiang Tethys, *Mineral Deposits (in Chinese)*, 29, 1, 37-42, doi: 10.16111/j.0258-7106.2010.01.007.
- Gao, Y. and S. Zheng (1995). Cross correlation function analysis of shear wave splitting: method and example of its application, *J. Earthquake Pred. Res.*, 4, 224-237.
- Gao, Y., A. Chen, Y. Shi, Z. Zhang and L. Liu (2019). Preliminary analysis of crustal shear-wave splitting in the Sanjiang lateral collision zone of the southeast margin of the Tibetan Plateau and its tectonic implications, *Geophys. Prosp.*, 67, 9, 2432-2449, doi: 10.1111/1365-2478.12870.

- Gao, Y., J. Wu, G. Yi and Y. Shi (2010). Crust-mantle coupling in North China: Preliminary analysis from seismic anisotropy, *Chinese Sci. Bull.*, 55, 3599-3605, doi: 10.1007/s11434-010-4135-y.
- Gao, Y., J. Wu, Y. Fukao, Y. Shi and A. Zhu (2011). Shear-wave splitting in the crust in North China: Stress, faults and tectonic implications, *Geophys. J. Int.*, 187, 2, 642-654, doi: 10.1111/j.1365-246X.2011.05200.x.
- Gao, Y., P. Wang, S. Zheng, M. Wang, Y. Chen and H. Zhou (1998). Temporal changes in shear-wave splitting at an isolated swarm of small earthquakes in 1992 near Dongfang, Hainan Island, southern China, *Geophys. J. Int.*, 135, 1, 102-112, doi: 10.1046/j.1365-246X.1998.00606.x.
- Gao, Y., Y. Shi and Q. Wang (2020). Seismic anisotropy in the southeastern margin of the Tibetan Plateau and its deep tectonic significances, *Chinese J. Geophys.* (in Chinese), 63, 3, 802-816, doi: 10.6038/cjg202000003.
- Gao, Y., Q. Wang, B. Zhao and Y. Shi (2014). A rupture blank zone in middle south part of Longmenshan Faults: Effect after Lushan Ms7.0 earthquake of 20 April 2013 in Sichuan, China, *Science China Earth Sci.*, 57, 9, 2036-2044, doi: 10.1007/s11430-014-4827-2.
- He, C., C. Wang and J. Wu (2004). A study on deep structure using teleseismic receiver function in Western Yunnan, *Acta Seismologica Sinica (English Edition)*, 17, 262-271, doi: 10.1007/s11589-004-0048-7.
- Hu, J., Y. Su, X. Zhu and Y. Chen (2003). S-wave velocity and Poisson's ratio structure of crust in Yunnan and its implication, *Science China Earth Sci.*, 48, 210-218, doi: 10.1360/03yd0062.
- Hua, W., J. Liu, Z. Chen and S. Zheng (2006). Study on S wave splitting in Dayao earthquake sequence with $M = 6.2$ and $M = 6.1$ in Yunnan in 2003, *Acta Seismologica Sinica (English Edition)*, 19, 380-396, doi: 10.1007/s11589-004-0380-1.
- Huangfu, G., S. Shi and Y. Su (2000). Study on seismicity in Yunnan in the 20th century, *J. Seismol. Res.* (in Chinese), 23, 1, 1-9.
- Jin, H., Y. Gao, X. Su and G. Fu (2019). Contemporary crustal tectonic movement in the southern Sichuan-Yunnan block based on dense GPS observation data, *Earth Planet. Phys.*, 3, 1, 53-61, doi: 10.26464/epp20190006.
- Kan, R., S. Zhang, F. Yan and L. Yu (1977). Present tectonic stress field and its relation to the characteristics of recent tectonic activity in southern China, *Chinese J. Geophys.* (in Chinese), 20, 2, 96-109.
- Kaviris, G., I. Spingos, C. Millas, V. Kapetanidis, I. Fountoulakis, P. Papadimitriou, N. Voulgaris and G. Drakatos (2018). Effects of the January 2018 seismic sequence on shear-wave splitting in the upper crust of Marathon (NE Attica, Greece), *Phys. Earth Planet. Int.*, 285, 45-58, doi: 10.1016/j.pepi.2018.10.007.
- Kaviris, G., I. Spingos, V. Kapetanidis, P. Papadimitriou and N. Voulgaris (2021). On the origin of upper crustal shear-wave anisotropy at Samos Island, Greece, *Acta Geophys.*, 69, 1051-1064, doi: 10.1007/s11600-021-00598-2.
- Kaviris, G., I. Spingos, V. Kapetanidis, P. Papadimitriou, N. Voulgaris and K. Makropoulos (2017). Upper crust seismic anisotropy study and temporal variations of shear-wave splitting parameters in the western Gulf of Corinth (Greece) during 2013, *Phys. Earth Planet. Int.*, 269, 148-164, doi: 10.1016/j.pepi.2017.06.006.
- Lei, J., P. Wang, C. Yao and Y. Chen (1997). The Near-field shear wave splitting and its relation with structure in Jianchuan, Yunnan province, *Chinese J. Geophys.* (in Chinese), 40, 6, 791-801.
- Li, L., X. Liu, Y. Wan and Z. Zheng (2021). Crustal deformation characteristics and recent movement changes of main fault zones in northwest Yunnan revealed by GPS and numerical simulation, *Acta Geologica Sinica (in Chinese)*, 95, 11, 3205-3219.
- Li, Q., S. Feng, Z. Bai, Y. Gao, S. Gao, X. Xiong, X. Wang, C. Lang, R. Han, Q. Wu, Z. Lu, H. Wang, W. Li, H. Zhang and X. Zhang (2018). New research progress on crust-upper mantle structure in the southeastern margin of Qinghai-Tibet Plateau, China, *J. Earth Sci. Environ.* (in Chinese), 40, 6, 757-778.
- Li, X. and Y. Gao (2022). Tectonics and lithospheric anisotropy in the Sanjiang lateral collision zone of the SE margin of the Tibetan plateau, *Progress in Geophys.* (in Chinese), 37, 4, 1431-1447, doi: 10.6038/pg2022FF0421.
- Liu, G., Y. Gao and Y. Shi (2015). Crustal anisotropy in the southeast of the Yunnan-Guizhou Plateau, China, *Earthquake (in Chinese)*, 35, 3, 76-85.
- Müller, M. C. (1991). Prediction of lateral variability in fracture intensity using multi-component shear-wave surface seismic as a precursor to horizontal drilling in the Austin Chalk, *Geophys. J. Int.*, 107, 3, 409-415, doi: 10.1111/j.1365-246X.1991.tb01402.x.
- Pan, G., Li. Wang, Rong. Li, Si. Yuan, Wen. Ji, Fu. Yin, Wan. Zhang and Bao. Wang (2012). Tectonic evolution of the Qinghai-Tibet Plateau, *J. Asian Earth Sci.*, 53, 3-14, doi: 10.1016/j.jseaes.2011.12.018.
- Qian, X., J. Qin and L. Liu (2011). Study on recent tectonic stress field in Yunnan region, *Seismol. Geol.* (in Chinese), 33, 1, 91-106, doi: 10.3969/j.issn.0253-4967.2011.01.009.

- Royden, L. H., B. C. Burchfiel and R. D. van der Hilst (2008). The geological evolution of the Tibetan Plateau, *Science*, 321, 1054-1058, doi: 10.1126/science.1155371.
- Sheng, S., X. Hu, X. Wang, Y. Wan, H. Li, Z. Li, X. Tian, X. Wang and S. Zhang (2022). Study on the crustal stress field of Yunnan and its adjacent areas, *Chinese J. Geophys.* (in Chinese), 65, 9, 3252-3267, doi: 10.6038/cjg2022p0536.
- Shi, Y., Y. Gao, J. Wu and Y. Su (2009). Crustal seismic anisotropy in Yunnan, Southwestern China. *Journal of Seismology*, 13, 2, 287-299, doi: 10.1007/s10950-008-9128-9.
- Shi, Y., Y. Gao, X. Shen and K. H. Liu (2020). Multiscale spatial distribution of crustal seismic anisotropy beneath the northeastern margin of the Tibetan plateau and tectonic implications of the Haiyuan fault, *Tectonophysics*, 774, 228274, doi: 10.1016/j.tecto.2019.228274.
- Sun, Y., X. Zhao, Y. Huang, H. Yang and F. Li (2017). Characteristics of focal mechanisms and stress field of Yunnan area, *Seismol. Geol.* (in Chinese), 39, 2, 390-407.
- Tai, L., Y. Gao, G. Liu and Z. Xiao (2015). Crustal seismic anisotropy in the southeastern margin of Tibetan Plateau by ChinArray data: shear-wave splitting from temporary observations of the first phase, *Chinese J. Geophys.* (in Chinese), 58, 11, 4079-4091, doi: 10.6038/cjg20151116.
- Tapponnier, P., G. Peltzer, A. Y. Le Dain, R. Armijo and P. Cobbold (1982). Propagating extrusion tectonics in Asia: New insights from simple experiments with plasticine, *Geology*, 10, 12, 611-616, doi: 10.1130/0091-7613(1982)10<611:PETIAN>2.0.CO;2.
- Tian, J., Y. Luo and L. Zhao (2019). Regional stress field in Yunnan revealed by the focal mechanisms of moderate and small earthquakes, *Earth Planet. Phys.*, 3, 3, 243-252, doi: 10.26464/epp2019024.
- Wang, D., Y. Dong, Q. Jiao, D. Zhang, J. Duan and H. Yu (2022). The mechanism of tectonic deformation of the Central Yunnan Terrane in the late Cenozoic based on tectonic geomorphology, *Earth Science* (in Chinese), 47, 8, 3016-3028, doi: 10.3799/dqkx.2021.146.
- Wang, M. and Z. Shen (2020). Present-day crustal deformation of continental China derived from GPS and its tectonic implications. *Journal of Geophysical Research: Solid Earth*, 125, e2019JB018774, doi: 10.1029/2019JB018774.
- Wang, Y., Y. Wang, P. Zhang, J. Zhang, B. Zhang, J. Liu, R. Zhou, W. Wang, H. Zhang and C. Liu (2022). Cenozoic tectonic evolution of regional fault systems in the SE Tibetan Plateau, *Science China Earth Sciences* (in Chinese), 65, 4, 601-623, doi: 10.1007/s11430-021-9880-3.
- Wu, C., H. Fu and J. Liu (2006). Shear wave splitting of aftershocks with $M = 6.2$ and 6.1 after Dayao earthquake in Yunnan 2003, *Earthquake* (in Chinese), 26, 1, 1-9.
- Wu, C., J. Qin and G. Huangfu (2004). Shear wave splitting of aftershocks of $M6.0$ Yongsheng earthquake, *J. Seismol. Res.* (in Chinese), 27, 2, 140-145.
- Wu, J., Y. Ming and C. Wang (2001). The S wave velocity structure beneath digital seismic stations of Yunnan province inferred from teleseismic receiver function modelling, *Chinese J. Geophys.* (in Chinese), 44, 2, 228-237+295.
- Wu, J., Y. Ming and C. Wang (2004). Source mechanism of small-to-moderate earthquakes and tectonic stress field in Yunnan province, *Acta Seismologica Sinica* (in Chinese), 26(5), 457-465.
- Xu, X., Z. Han and G. Zhang (2016). *Seismotectonic map in China and its adjacent regions*, Seismological Press, Beijing (in Chinese).
- Xu, Z., J. Yang, W. Li, L. Zeng and C. Xu (2012). Tectonic background of important metallogenic belts in the southern and southeastern Tibetan Plateau and ore prospecting, *Acta Geologica Sinica* (in Chinese), 86, 12, 1857-1868.
- Xu, Z., S. Wang, Y. Huang, A. Gao, X. Jin and X. Chang (1987). Directions of mean stress axes in southwestern China deduced from microearthquake data, *Chinese J. Geophys.* (in Chinese), 30, 5, 476-486.
- Yin, F., Y. Tang and B. Xu (2021). Cenozoic strike slip orogeny in Sanjiang area, southwestern China, *Sedimentary Geology and Tethyan Geology* (in Chinese), 41, 1, 1-14, doi: 10.19826/j.cnki.1009-3850.2020.04001.
- Zhang, P., Q. Deng, G. Zhang, J. Ma, W. Gan, W. Min, F. Mao and Q. Wang (2003). Active tectonic blocks and strong earthquakes in the continent of China, *Science China Earth Sci.*, 46, Suppl 2, 13-24, doi: 10.1360/03dz0002.
- Zhang, Z. and Y. Gao (2019). Crustal thicknesses and Poisson's ratios beneath the Chuxiong-Simao Basin in the Southeast Margin of the Tibetan Plateau, *Earth Planet. Phys.*, 3, 1, 69-84, doi: 10.26464/epp2019008.

*CORRESPONDING AUTHOR: Yuan GAO,

Key Laboratory of Earthquake Prediction, Institute of Earthquake Forecasting, China Earthquake Administration,
Beijing 100036, China
e-mail: qzgyseis@163.com